Clim. Past Discuss., 9, 2929–2966, 2013
www.clim-past-discuss.net/9/2929/2013/
doi:10.5194/cpd-9-2929-2013

Climate of the Past Discussions
Open Access

Inferred changes in El Niño-Southern Oscillation variance over the past six centuries

S. McGregor[1,2], **A. Timmermann**[3], **M. H. England**[1,2], **O. Elison Timm**[3], **and A. T. Wittenberg**[4]

[1]Climate Change Research Centre, University of New South Wales, Sydney, Australia
[2]ARC Centre of Excellence for Climate System Science, University of New South Wales, Sydney, Australia
[3]International Pacific Research Centre, University of Hawaii, Honolulu, Hawaii, USA
[4]Geophysical Fluid Dynamics Laboratory/NOAA, Princeton, New Jersey, USA

Received: 6 May 2013 – Accepted: 11 May 2013 – Published: 30 May 2013

Correspondence to: S. McGregor (shayne.mcgregor@unsw.edu.au)

Published by Copernicus Publications on behalf of the European Geosciences Union.

Abstract

It is vital to understand how the El Niño–Southern Oscillation (ENSO) has responded to past changes in natural and anthropogenic forcings, in order to better understand and predict its response to future greenhouse warming. To date, however, the instrumental record is too brief to fully characterize natural ENSO variability, while large discrepancies exist amongst paleo-proxy reconstructions of ENSO. These paleo-proxy reconstructions have typically attempted to reconstruct the full temporal variability of ENSO, rather than focusing simply on its variance. Here a new approach is developed that synthesizes the information on common low frequency variance changes from various proxy datasets to obtain estimates of ENSO variance. The method is tested using surrogate data from two coupled general circulation model (CGCM) simulations. It is shown that in the presence of dating uncertainties, synthesizing variance information provides a more robust estimate of ENSO variance than synthesizing the raw data than identifying its running variance. We also examine whether good temporal correspondence between proxy data and instrumental ENSO records implies a good representation of ENSO variance. A significant improvement in reconstructing ENSO variance changes is found when combining several proxies from diverse ENSO-teleconnected source regions, rather than by relying on a single well-correlated location, suggesting that ENSO variance estimates provided derived from a single site should be viewed with caution. Finally, identifying the common variance signal in a series of existing proxy based reconstructions of ENSO variability over the last 600 yr we find that the common ENSO variance over the period 1600–1900 was considerably lower than during 1979–2009.

CPD
9, 2929–2966, 2013

1 Introduction

The El Niño–Southern Oscillation (ENSO) is characterized by variations in sea surface temperature (SST) in the eastern tropical Pacific, causing changes in ocean currents and atmospheric circulation patterns globally. Related shifts in wind and rainfall patterns can lead to changes in extreme events including flooding, droughts, and tropical cyclone activity (Chan, 1985; Larkin and Harrison, 2002; Nicholls, 1985; Power et al., 1999). ENSO has been shown to exhibit significant multi-decadal variability in its strength and frequency throughout the instrumental period (Power, et al., 1999; Timmermann et al., 2003; Zhang et al., 1998), with additional longer-term variability reported in proxy data (Li et al., 2011; Wolff et al., 2011; Emile-Geay et al., 2013b).

Characterizing ENSO's long-term changes in frequency, magnitude and duration has been hampered by the fact that reliable instrumental records cover a period of less than 150 yr. This period is too brief to capture the range of long-term changes in ENSO frequency, magnitude and duration (Wittenberg 2009). Multi-century paleo climate reconstructions derived from monthly to annually resolved tree rings, ice cores, lake sediments and coral records can be used to extend the observational record and to further quantify ENSO's sensitivity to external radiative perturbations in the "backdrop" of its internally generated variability (Federov and Philander 2000). Numerous attempts have been made to reconstruct ENSO variability back in time using various paleo-proxy archives (e.g., see Table 1). A comparison of the corresponding multi-decadal to centennial-scale ENSO variance changes (Fig. 1) reveals a high degree of uncertainty which reduces our confidence in how well any individual reconstruction can in fact capture low frequency ENSO variance modulations.

In this study we use two multi-century-long coupled general circulation model (CGCM) simulations to examine an assumption made implicitly by many paleo-reconstruction studies – i.e., that a good temporal correspondence between a given climate variable and ENSO translates also into a high correlation between multi-decadal variance changes in this variable and in ENSO. We also test a simple method to extract

CPD
9, 2929–2966, 2013

the common ENSO variance modulation signal using proxies from a variety of ENSO-teleconnected locations that is robust against small dating errors, unlike previous proxy analyses. We then use this method to identify the common variance signal in a number of pre-defined proxy-based ENSO reconstructions and a range of single station rainfall and temperature proxies over the past 600 yr.

2 Simulations

The CGCM simulations used in this study are the externally forced Last Millennium (850–1850) simulation of the Community Climate System Model, version 4 (hereafter CCSM4, Landrum et al., 2013) and a 2000 yr pre-industrial control run of the Geophysical Fluid Dynamics Laboratory (GFDL)-CM2.1 model with no changes in external forcings (Wittenberg 2009). Note that prior to any analysis, annual mean (July–June) values of model precipitation and Surface Temperature (T_S) data from the model simulations are calculated, and the resulting time series are high pass filtered (HPF) with a 10 yr cutoff to focus on the interannual variability.

The atmospheric component of CCSM4 uses a uniform horizontal resolution of 1.258 in latitude by 0.98 in longitude and has 26 layers in the vertical (Neale et al., 2013). The ocean model, which is based on version 2 of the Parallel Ocean Program model (Smith et al., 2010), uses the standard ocean grid with a displaced grid North Pole, nominal 1° horizontal resolution (uniform 1.18 in longitude, variable in latitude from 0.27° at the equator to 0.54° at 33° latitude), and 60 levels in the vertical (Danabasoglu et al., 2012). The land surface model adopts to the same horizontal resolution as CAM4, while the sea ice model uses the same horizontal grid as the ocean component (Landrum et al., 2013). CCSM4's simulation of tropical Pacific climate is described extensively in Deser et al. (2012). It is characterized by a realistic seasonal evolution of atmospheric and oceanic fields, realistic asymmetry between El Niño and La Niña events, and a realistic pattern of teleconnections.

CPD
9, 2929–2966, 2013

The CM2.1 ocean model is based on Modular Ocean Model version 4 (MOM4) code, with 50 vertical levels and a 1° × 1° horizontal resolution that telescopes to 1/3° meridional spacing near the equator. The atmospheric component has 24 vertical levels, 2° latitude by 2.5° longitude horizontal resolution. The land surface model has the same horizontal resolution as the atmosphere. Full model details can be found in Delworth et al. (2006). CM2.1 has a robust ENSO which includes realistic multidecadal fluctuations in amplitude, an irregular period between 2–5 yr, and SST anomalies that are skewed toward warm events as observed. The evolution of ENSO subsurface temperatures is quite realistic, as are ENSOs teleconnections as represented by correlations with precipitation anomalies outside the tropical Pacific. CM2.1s tropical climate and variability is extensively described in Wittenberg et al. (2006).

3 Methods

3.1 Testing the running variance implications of a good temporal correlation

The fact that there is such a wide spread between the running variances of the individual ENSO reconstructions (Fig. 1) raises the question whether a good temporal correspondence between a given regional climate variable and ENSO can be used to imply that the variable will also provide a good representation of ENSO variance. We use output from the CCSM4 and CM2.1 models to address this question. Calculating the correlation between the simulated CM2.1 running variance of T_S with the running variance of the modeled ENSO (Fig. 2a, shading), represented by the Nino 3.4 area-averaged (5° S–5° N, 120° W–170° W) sea surface temperature anomalies (SSTA), and comparing it with the absolute value of the correlation between anomalies of T_S and modeled ENSO (Fig. 2a, contours) reveals a strong similarity between the two maps of correlation coefficients. Note, here and elsewhere in this manuscript that the running variance is calculated in a 30 yr sliding window. This similarity is reflected by the spatial correlation coefficient of 0.79 (r^2 = 0.63) calculated between the two spatial maps.

CPD
9, 2929–2966, 2013

Similar results are also obtained when the same calculations are performed on the CCSM4 simulation output (Fig. 2c) and again this is reflected by the spatial correlation of 0.70 ($r^2 = 0.49$) calculated between the two spatial maps. This implies that a large absolute value of the correlation between T_S and ENSO provides a clear indication that the running variance of T_S will track that of ENSO reasonably well.

Carrying out the same analysis for CM2.1 and CCSM4 precipitation data reveals some interesting differences between the running variance (precipitation running variance – ENSO running variance) correlation patterns and the raw (precipitation – ENSO) correlation patterns in the tropical Pacific (Fig. 2b and d). These differences between the correlation maps are reflected by the spatial correlations (r) of 0.67 ($r^2 = 0.45$) and 0.55 ($r^2 = 0.31$) respectively.

Figure 3 displays the 5th, 50th and 95th percentiles of the correlation coefficients calculated between the running variance of precipitation for all grid points and the running variance of ENSO binned according to the correlation between precipitation and ENSO. As expected from the significant differences between the two maps displayed in Fig. 2, the 5th percentile curve reveals that having a strong correlation between precipitation and ENSO at a particular location does not guarantee a strong correlation between the running variance of precipitation and the running variance of ENSO. For instance, in CM2.1 if a precipitation signal is selected that has an r^2 value of between 0.6 and 0.7 when compared with the time series of ENSO SSTAs, there is a 10 % chance that the running variance of that precipitation time series will have no significant correlation ($r < 0.31$ or $r^2 < 0.1$) with the running variance of ENSO (Fig. 3a). This indicates that ENSO may influence the sign and timing of the rainfall change at this location, however unrelated processes influence the magnitude of that change.

We find that a strong correlation between the common precipitation signal, averaged over two or more different locations and ENSO is a much better indicator for a high correlation between the running variance of the median (common) precipitation data and the running variance of ENSO (Fig. 3a) as compared to the case with only one location. For instance, if we pick two geographic locations for which the median (common)

CPD
9, 2929–2966, 2013

precipitation signal has an r^2 of between 0.6 and 0.7 with ENSO, there is only a 1 % chance that that the running variance of that common precipitation time series will have no significant correlation ($r < 0.31$ or $r^2 < 0.1$) with the running variance of ENSO. This is 10 times less likely than the case with precipitation data only sourced from one location. This result is consistent with CCSM4 data which suggests a common precipitation signal, from two geographic locations that have r^2 of > 0.7 when compared to ENSO SSTA, will make it 3.5 times less likely that the running variance of that signal will have no significant correlation ($r < 0.3$ or $r^2 < 0.1$) with the running variance of ENSO (Fig. 3b).

We note that there are several issues with this type of analysis. The first is that a large number of the proxies are sensitive to both temperature and rainfall (e.g., Cobb et al., 2003); the second issue is that all models have biases in the mean state, and ENSO's modeled teleconnections can be spatially shifted compared to observations – possibly implying biases in the spatial locations of the regions where the anomaly and running variance correlations with ENSO differ. We note, however, that both simulations suggest that these regions (i.e., where rainfall is moderately correlated with ENSO, while the running variance displays little correlation with the running variance of ENSO) are in, or very close to, ENSO's centre of action in the western tropical Pacific.

Regardless of these model issues, these results suggest: (i) a strong correlation between T_S and ENSO provides a clear indication that the running variance of T_S is likely to track that of ENSO; (ii) a strong correlation between precipitation and ENSO at a particular location does not guarantee a strong correlation between the running variance of precipitation and the running variance of ENSO. As such, ENSO variance estimates provided by reconstructions derived from precipitation sensitive proxies at a single site should be viewed with caution; and (iii) a multi-site common precipitation signal which is strongly correlated with ENSO provides much better indication that the common precipitation signal's running variance will be related to the running variance of ENSO.

CPD
9, 2929–2966, 2013

3.2 Identifying the common variance signal

A previous study has shown that the linear combination of many of the above listed individual eastern equatorial Pacific reconstructions can further increase the signal-to-noise ratio compared with the individual reconstructions (McGregor et al., 2010). However, it was noted that the variance changes of this combined proxy product appeared to show the effects of dating errors towards the beginning of the 350 yr record. Similar dating errors have also been noted in studies that attempt to reconstruct observed ENSO over the last 1000 yr (Emile-Geay et al., 2013a,b). This is a concern because proxies displaying small dating errors can act to cancel out the common signal when combined; hence artificially reducing the combined signal variance.

3.2.1 Methods for identifying the common variance signal

Here we will examine whether identifying the median of the running variance signals (MRV) of numerous source proxies (e.g., median ($\sigma^2(P_x(t))$)) is equivalent to identifying the running variance of the median signal (RVM) (e.g., $\sigma^2(\text{median}(P_x(t)))$) in the absence of dating errors. The source proxy timeseries are abbreviated as P_x(t). This will be accomplished by analyzing the output from the CCSM4 and CM2.1 models. To this end, we select x ($x = 1,2,3,\ldots,9$) time series of either precipitation or T_S from random global locations, with the only constraint on the location being that its time series must have a absolute correlation coefficient > 0.3 when compared to modeled ENSO variability (again ENSO variability is calculated as average SSTA in the Niño 3.4 region). We then calculate the MRV and RVM of the x time series. Note again that the running variance is calculated in a 30 yr sliding window. The above procedure is repeated until we obtain 10 000 MRVs and 10 000 RVMs for each x representing either precipitation or surface temperature.

Plotting the 5, 50 and 95 percentiles of the correlation coefficients calculated between ENSO running variance and the MRV as a function of x, along with the corresponding values calculated between ENSO running variance and the RVM reveals that

CPD
9, 2929–2966, 2013

the percentiles of the two derivation methods are very similar for both fields in both models (Fig. 4). This is also confirmed by plotting the correlation coefficients calculated between ENSO running variance and the RVM against the corresponding ENSO running variance and MRV correlation coefficients (Fig. 5a and c). This indicates that while both methods will provide different estimates of the ENSO running variance time series, MRV is roughly equivalent to RVM in the absence of dating errors.

Furthermore, all percentiles increase as x increases, indicating that as number of proxies (x) increases the common signal is more likely to provide a skillful estimate of ENSO running variance. This confirms one of the initial assumptions used in many paleo climate studies that a network of proxies helps to reduce the effects of biases, noise, and weaknesses in the individual indicators (Mann et al., 2000).

3.2.2 The effect of dating errors on the common running variance signal

Here we examine whether calculating the median individual proxy running variance time series (MRV), as opposed to calculating the running variance of the median of the proxy time series (RVM), reduces the effects of dating uncertainties in the reconstructions of ENSO variance changes as proposed by McGregor et al. (2010). To this end, five sets of precipitation time series are extracted from the CM2.1 simulation, which include all precipitation time series that have the absolute value of the correlation coefficients > 0.3 with modeled average SSTA in the Niño 3.4 region. In four of these five sets, the entire time series is shifted by between 1–5 yr to mimic a dating error. What varies between these four sets, however, is the ratio of the time series that is subject to the introduced temporal shift, changing from 1/5, 1/4, 1/3, and 1/2.

Using these data and the approach outlined above in Sect. 3.2.1, we select x ($x = 1, 2, 3, \ldots, 9$) precipitation time series from one of these data sets and then calculate the MRV and RVM. The 5, 50 and 95 percentiles of the correlations calculated between ENSO running variance and the MRV for each of the five data sets as a function of x, reveal that the introduced temporal shifts have virtually no effect on the estimates of ENSO's running variance time series identified by the MRV method (Fig. 6a). On

CPD
9, 2929–2966, 2013

the other hand, plotting the same percentiles for the correlations calculated between ENSO running variance and the RVM signal (e.g., σ^2 (median($P_x(t)$))) reveals that the introduced temporal shifts have a large effect on the estimates of running variance identified by the RVM method (Fig. 6b).

This clearly indicates that the MRV method provides a much more robust estimate of ENSO's running variance than the RVM method when dating errors are present in the input time series. We note that this result remains consistent regardless of the model (CM2.1 or CCSM4) or the output field used (i.e., precipitation or T_S).

4 Application to existing ENSO proxy reconstructions

Here we examine the MRV of the 14 existing ENSO reconstructions listed in Table 1 and presented in Fig. 1[1]. Each of these reconstructions is based on current and paleo-proxy data sources from a range of geographic regions, with a variety of statistical methods used in the derivation of the relevant indices (see Table 1 and references therein). Considering that we have shown that the multi-proxy approach minimizes the impact of weaknesses in any individual proxy (Sect. 3.2.1), it is expected that the use of this wide network of ENSO proxies will allow us to reconstruct the long-term changes in past ENSO variance with greater statistical skill than available from individual reconstructions alone.

Here we focus on the interannual ENSO frequency by high-pass filtering (10 yr cutoff period) each of the 14 ENSO reconstructions. Each of these filtered time series are then normalized using the base period 1900–1977 for the calculation of standard deviation and a time series of thirty-year-sliding-window running variance is calculated for each reconstruction. The running variance time series are then adjusted by adding a constant, such that their mean running variance over the period 1900–1977 matches

[1]The term "existing ENSO reconstructions" refers to ENSO reconstructions (see Table 1) that have been previously defined in the scientific literature. These reconstructions often use proxy data from multiple locations and rely on statistical methods to extract the ENSO signal.

CPD
9, 2929–2966, 2013

that of the high-pass filtered observed N34 index over the same period. As shown in Fig. 1, there is a large spread between the running variances that highlight the discrepancies amongst the ENSO reconstruction variances (Fig. 7).

Comparing the MRV of the ENSO proxy reconstructions with the 30 yr running variance of the high pass filtered (10 yr cutoff) ENSO signal derived from direct observations during the instrumental period reveals a remarkable correspondence (Fig. 7). This further increases the confidence in the ensemble averaging technique applied here to the running variance. Figure 7 also reveals that the observed amplitude in the most recent 30 yr of the 20th Century (1979–2009, indicated by the red star) appears to have been larger than at any time during the preceding multi-century MRV record.

We note that the number of ENSO time series taken into account when calculating the MRV signal varies with time, depending on the length and span of the individual records (Fig. 7, Table 1). Error bars are calculated using two separate pseudo-proxy methods, such that the length of the error bar varies in relation to the number of available ENSO proxies (see Appendix A). For instance, with fewer proxies available (e.g. during the period 1400–1500) the estimators of the running variance become more uncertain than for a period (e.g. the 1800s) where many more proxy time-series overlap. At any point in time the most conservative (widest) error bar of the two pseudo proxy methods is displayed in Fig. 7.

The increased variance of ENSO for the most recent 30 yr is significantly larger (exceeding the 95 % confidence level) than at any time during the past ~ 400 yr (i.e., the observed variance, indicated by the red star, is larger than the median proxy signal error bars in the period from the year 1590 through to the start of the instrumental data). Prior to this period, the uncertainty range of the MRV signal, estimated by the error bars, is too large to be conclusive.

4.1 Independence of existing ENSO proxy reconstructions

We note that some of the input proxy networks overlap among these 14 ENSO reconstructions (see Appendix B for a more in depth discussion), such that they are not

CPD
9, 2929–2966, 2013

always completely independent in a geographical sense. In spite of geographical overlap for some of the reconstructions, usually different statistical methods are applied to tease out the ENSO signal. These methods range from simply calculating an Empirical Orthogonal Function (EOF) of the input proxy network (e.g., Braganza et al., 2009; McGregor et al., 2010; Li et al., 2011) to the more complex method of regressing proxy data onto the leading spatio-temporal eigenmodes of observed data (e.g., Mann et al., 2000; Evans et al., 2002; Cook 2008).

Despite the methodological differences, this apparent lack of independence raises the concern that the *noise*, i.e. the non-ENSO component of these overlapping input proxies, may distort or mask the common ENSO signal and this could be incorrectly attributed to changes in ENSO. If this were true, we would expect the *noise* influencing tropical coral-dependent reconstructions to be distinct from that of North American tree rings. As such, if the running variance of either or both of these groups' reconstructions were dominated by noise we would expect to see significant differences in their common variance signal. However, this is not the case. Identifying the common variance signal in only those reconstructions with common tropical corals reveals a post-1700 signal that is extremely similar to that identified in only those reconstructions with common North American tree rings (Fig. 8), thus lending further support of the RMV method applied here. In addition, both of the above signals resemble the common variance signal identified in the full set of ENSO reconstructions. This gives us confidence that the common variance signal identified in this study is not strongly distorted or dominated by independent *noise*. We note that reconstructions 3 and 9 include common tropical corals and North American tree rings; however, neglecting these two reconstructions from both of the above subsets leaves the common variance signals virtually unchanged (figure not shown).

CPD
9, 2929–2966, 2013

5 Application to observed single station proxies

It is also noted here that by using existing ENSO reconstructions that exhibit high correlations with the N34 observations during the instrumental period, we have attempted to consolidate the common information contained within these reconstructions rather than defining another reconstruction to add to the literature. However, as the reconstructions in most cases have already incorporated information from numerous time series, artificial variance reduction due to dating errors in the source proxies may already be incorporated into our analysis. As such, we may not be getting the best out of the methodological advantage of combining running variances when applying it to these synthesized time series.

Thus, here we also examine the common running variance signal in a range of single location proxies and compare the results with those derived above (Table 3). Again we focus on the interannual ENSO frequency by high-pass filtering (10 yr cutoff period) each of the proxies. We utilize all tree ring proxies listed by Emile-Geay et al. (2013a, b) and all tropical Pacific coral proxies available from the NOAA National Climate Data Centre (NCDC) that continuously span the period 1800–1980. However, prior to their inclusion in Table 3, these proxies were pre-screened to ensure they have a correlation of at least 0.3 when compared with the annual mean (July–June) observations of ENSO from any of the four SST products used in Table 4. Each of these filtered time series are then normalized over the 1900–1977 period and a time series of running variances, in a thirty year sliding window, is calculated for each reconstruction. The variance time series are then adjusted by adding a constant, such that their mean running variance over the period 1900–1977 matches that of the high-pass filtered observed N34 index over the same period.

Calculating the common variance signal of all proxies listed in Table 3 reveals a time series that displays a good correspondence to the observed high pass filtered ENSO running variance signal (Fig. 8a inset). This common variance time series falls well within the error estimates of the 14 existing ENSO reconstructions presented in Sect. 4

CPD
9, 2929–2966, 2013

(Table 1). In fact, comparing this common running variance time series with that of the 14 existing ENSO reconstructions reveals a strong similarity through most of the 600 yr period (Fig. 9a).

Using only the 12 tree ring proxies (sourced from Emile-Geay et al., 2013; Table 3) we calculate the MRV signal. Comparing this running variance signal with that of the observed high pass filtered ENSO signal reveals a good correspondence (Fig. 8b inset). Again, this common variance time series falls well within the error estimates of the 14 existing ENSO reconstructions, and directly comparing this common running variance time series with that of the 14 existing ENSO reconstructions, reveals a strong similarity through most of the 600 yr period (Fig. 8b).

Calculating the MRV signal of the 9 coral proxies from Table 3, and comparing this running variance signal with that of the observed HPF ENSO signal reveals some correspondence (Fig. 8c inset), although the correlation appears much weaker than for the individual tree-ring records (Fig. 8b inset). The correspondence is most notable prior to 1960; after this time the observed RV begins to steadily increase while the coral MRV signal remains relatively constant. The facts that (i) the coral MRV signal does not pick up the increase in ENSO variance since the mid-1900s; and (ii) there is very little correspondence between this signal and the ENSO proxy reconstruction MRV time series outside of the period 1850–1950 (Fig. 8c); reduces our confidence in this signal, which is namely sourced from the southwestern tropical Pacific, as it relates to ENSO. As the southwestern tropical Pacific is home to the South Pacific Convergence Zone (SPCZ), a possible explanation for these discrepancies could be that there may have been slow shifts in the tropical Pacific temperature/rainfall covariance that could have affected some of the δ^{18}O-based coral proxies in this region. However, in spite of this, the coral common variance time series falls mostly within the error estimates of the ENSO proxy reconstruction MRV signal.

Thus, consistent with the analysis of existing ENSO reconstructions presented in Fig. 7, the common running variance signal of the Table 3 single station proxies (whether they are based on all data or solely on coral or tree ring data) reveals that the

CPD
9, 2929–2966, 2013

observed amplitude in the most recent 30 yr of the 20th Century (indicated by the red star) appears to have been larger than at any time during the preceding multi-century record.

6 Summary and conclusions

The main goal of this study was to synthesize existing ENSO reconstructions to arrive at a better estimate of past ENSO variance changes. This is an important task since there are considerable discrepancies in ENSO variance estimates derived from the 14 available ENSO reconstructions that exhibit good correlations with the instrumental data (Figs. 1 and 7).

We first tested an implicit assumption of many ENSO reconstruction studies, namely, that if a proxy (whether it represents precipitation or surface temperature) represents ENSO variability well, it will also represent ENSO running variance well. Our results from the analysis of two independent multi-century CGCM simulations suggest that this assumption is valid for proxies of temperature variability, but not for single proxies of precipitation variability. That is, while local precipitation may be modulated by ENSO, its running variance might bear a much weaker correlation with ENSO's running variance. Thus, we recommend caution when inferring ENSO running variance from precipitation-sensitive proxy data from a geographically confined area, even if they are located in the central/eastern equatorial Pacific. Furthermore, we demonstrated that this effect is significantly reduced when a common precipitation signal is sourced from a range of geographic regions. That is, a common precipitation signal, which is strongly correlated with ENSO, provides a much better indication that the correlation between the rainfall running variance and ENSO running variance will also be strong.

We then showed that in the absence of dating errors, the median running variance signal (MRV) is roughly equivalent to calculating the running variance of the median signal (RVM). However, the latter method, which is commonly used in the literature, is

CPD
9, 2929–2966, 2013

much more sensitive to dating errors than the former. Importantly, these dating errors can lead to an artificial variance reduction due to the cancellation of the ENSO signal.

The results of our analysis also show that as the diversity of input proxies increases, the resulting common variance signal is more likely to provide a skillful estimate of ENSO running variance. This confirms one of the initial assumptions used in many paleo climate studies that a broad network of proxies helps to reduce the effects of biases and weaknesses in the individual indicators (Mann et al., 2000). Thus, we expect the MRV method to increase the signal to noise ratio of the ENSO variance changes, while minimizing the effects of dating uncertainties in the source proxies.

There are two important limitations of this study. Firstly, although our combined variance estimate is supported by the running variance signal calculated from uncalibrated single station corals (see Sect. 5), we do not assess the sensitivity of individual source ENSO reconstructions to their derivation and calibration techniques. A recent study has suggested that reconstructed centennial scale variability is particularly sensitive to the historical SST data set used during calibration (Emile-Gaey et al., 2013a,b). Secondly, we assume that the spatial structure of ENSO SSTA and ENSO's teleconnections do not change over time. This is a concern, as the single station proxies (Table 3) are largely sourced from regions considered teleconnected to ENSO and do not include any proxies from ENSO's centre of action in the eastern/central tropical Pacific. Thus, while the common running variance signals of these single station proxies support the synthesis of predefined ENSO reconstructions, the differences between the common running variance time series could reflect changes of teleconnection patterns over time (Fig. 9b and c).

With these potential limitations in mind, the synthesis of the fourteen predefined ENSO reconstructions (Table 1), along with the analysis of 21 single station proxy records (Table 3), suggests that the observed variance of ENSO over 1979–2009 was larger than at any time during the preceding 600 yr record. As a result of the large error bars in the estimates for the period prior to 1600 CE, however, the strong ENSO

CPD
9, 2929–2966, 2013

variance of the most recent 30 yr only exceeds the 95 % confidence level for the last ~ 400 yr.

Within the current methodology, sources of uncertainty could be reduced by (i) increasing the number of ENSO proxy reconstructions representing ENSO variability prior to 1600 CE; and/or (ii) increasing the number of annually resolved single station proxies that represent ENSO variability. The increase in single station proxies should preferably occur outside of the two regions most commonly used in ENSO reconstructions (Table 3), namely central/north America (tree rings) and the southwest tropical Pacific (corals).

Appendix A

Error bar calculation

The main goal of this pseudo-proxy technique is to assess how accurately the median of multiple pseudo-proxies can estimate the variance of the original proxies from which the pseudo-proxies are generated. Here we define the original source proxy as the "true" signal. To this end, each of the 14 normalized high-pass filtered proxy timeseries $p_i(t)(i = 1, \ldots, 14)$ (Table 1) is used as a "true" signal. Pseudo-proxies $\mathrm{pp}_{ij}(t) = p_i(t) + sz_j(t)(j = 1, \ldots J; J = 600)$ are generated by adding Gausian white noise $z_j(t)$ to the annual mean "true signal". The variance of $z_j(t)$ is randomly modulated by s, such that the correlation coefficient between the pseudo-proxy $\mathrm{pp}_{ij}(t)$ and the original proxy $p_i(t)$ (the "true" signal) is contained within the range of correlation coefficients between the original proxies and the instrumental SSTA signal (see Table 2). By definition, selecting numerous pseudo-proxies and averaging $(\mathrm{mean}(\mathrm{pp}_i(t)) = J^{-1} S_j \mathrm{pp}_{ij}(t))$ should allow for the "true" signal $p_i(t)$ to be identified, as the additive Gaussian white noise would cancel out if enough pseudo-proxies were utilized. If none of the proxy records had dating errors, the 30 yr running variance of $\mathrm{mean}(\mathrm{pp}_i(t))$ would match that of the "true proxy" $p_i(t)$. Unfortunately, the number of ENSO proxies is currently limited to 14, so

CPD
9, 2929–2966, 2013

averaging cannot completely attenuate the noise. Furthermore, the available proxy data will likely have dating errors leading to an artificial damping of the combined signal variance.

To bypass this signal cancellation issue, the 30 yr running variance of $pp_{ij}(t)$ is calculated, giving $pp^{rv}_{ij}(t)$. The variance of these $pp^{rv}_{ij}(t)$ time series are then adjusted by adding a constant, such that their mean running variance over the period 1900–1977 matches that of the "true proxy" over the same period. From this point two methods can be used to estimate the error bar for the running variance time series: (1) the first method generates $n = 5000$ groups for each proxy (i), that contains $m = 3$ randomly selected pseudo proxy running variance time series ($pp^{rv}_{ij}(t)$); and 5000 groups that contain $m = 4$ randomly selected pseudo proxy running variance time series ($pp^{rv}_{ij}(t)$); etc with m going up to 14). Hence the total number of realizations of pseudo-proxy running variances in this ensemble is $14 \times 102 \times 5000$, where $102 = \sum_{m=3}^{14} m$. The median of this set is then calculated with respect to m; e.g. for $m = 3, 4, \ldots, 14$, and for any given i we obtain the median over these m realizations in each of the 5000 groups => $mpp^{rv}_{imn}(t)$ giving a $14 \times 12 \times 5000$ matrix. Then for each i we calculate the error of these 5000 groups of median running variances with respect to the corresponding true running variance giving $\varepsilon^{rv}_{imn}(t) = p^{rv}_i t - mpp^{rv}_{imn}(t)$. The matrix $\varepsilon^{rv}_{imn}(t)$ is also of dimension 14 × 12 x 5000. To obtain an estimate of the uncertainty in running variances that can be applied to the median ENSO proxy variance presented here, and to maintain positive definiteness of the variance range, the following procedure is applied: the true proxy running variance as a function of time $p^{rv}_i(t)$ is split into $p = 8$ bins of equal width (going from 0.25 to 2) depending on the value of $p^{rv}_i(t)$; also the n corresponding error estimates ($\varepsilon^{rv}_{imn}(t)$) are binned into the same 8 equal bins => binned-$\varepsilon^{rv}_{imp}(q)$ is a $14 \times 12 \times 8 \times p$ matrix where the number of error estimates in each bin (q) is a multiple of n. For each bin and each proxy i the 5 and 95-percentiles of the realizations is computed within this bin. For each i and m there are now 8 sets of error bars, which depend on the magnitude of the corresponding true running variance signal. A conservative estimate of the error bars is obtained by taking the minimum or maximum of these 5

CPD
9, 2929–2966, 2013

and 95 percentiles, respectively, over all i. Depending on how many true proxies m are available at time t ($m = 3, \ldots, 14$), the corresponding proxy-variance magnitude-dependent conservative error bars are selected for the corresponding m to get the final proxy variance uncertainty range.

(2) The second method simply calculates the median of the $\mathrm{pp}_{ij}^{\mathrm{rv}}(t)$ over the i dimension, giving $m\mathrm{pp}_{j}^{\mathrm{rv}}(t)$. As the number of original proxy time series at any point in time is consistent with the magenta line in Fig. 3, this calculation directly provides 600 pseudo-estimates of the proxy median time series displayed in Fig. 2a (black line). The error bars calculated via this method implicitly incorporate the number of proxies used to estimate the variance at each time step and the magnitude of the signal it is trying to represent, so error bars are then calculated at each point in time by simply identifying the 5 % and 95 % levels.

As the addition of white noise to the pseudo-proxies acts to increase the mean variance of each pseudo-proxy time series, the shifting of each of the pseudo-proxy running variance time series by adding a constant (such that the mean of the last 100 yr matches that of the "true" signal $p_{j}^{\mathrm{rv}}(t)$) may act to shift the positive definite pseudo-proxy error bars towards more negative values; hence making it possible that the pseudo-proxy error bars include negative values. Such values will not be considered here, because of the positive definiteness of variances.

Appendix B

Proxy data independence

In Sect. 4, we noted that some of the input proxy networks used to develop these 14 ENSO reconstructions overlap. Neglecting reconstruction 10, which utilizes reconstructions 1–9 in its derivation along with the Urvina Bay corals (Dunbar et al., 1994), this input proxy data overlap can be broken down into two main groups, those utilizing:

CPD
9, 2929–2966, 2013

1. North American tree rings: very similar tree ring networks make up the entire input of two reconstructions (Numbers 7 and 13 in Table 1) and a subset (roughly 25 %) of this network is also used in reconstruction Number 2 (Cook, personal communication, 2009). Various subsets of this tree ring data are also utilized in reconstructions 1, 3, 4, 8 and 9.

2. Tropical corals:

    a. Corals from reconstruction number 6 (Table 1) are used in the Wilson et al. (2010) Centre Of Action (COA) reconstruction (Number 11 in Table 1).

    b. Urvina Bay (Dunbar et al., 1994) and Punta Pitt (Shen et al., 1992) corals are utilized in reconstructions 5 and 11.

    c. Clipperton Atol corals (Linsley et al., 2000) are utilized in reconstructions 9 and 11.

    d. Seychelles Island (Charles et al., 1997) and Espiritu Santo Island (Quinn et al., 1993) corals are utilized in reconstructions 5 and 12.

    e. The reconstruction of Mann et al. (2000) also uses Urvina Bay (Dunbar et al., 1994) and Espiritu Santo Island (Quinn et al., 1993) corals along with several other corals (e.g., Heiss 1994; Linsley et al., 1994) that are utilized in the Evans et al. (2002) reconstruction (Number 5).

Acknowledgements. S. McGregor and M. H. England are supported by the ARC. A. Timmermann and O. Elison Timm are supported by the Japan Agency for Marine-Earth Science and Technology (JAMSTEC) through its sponsorship of the International Pacific Research Center (IPRC).

CPD
9, 2929–2966, 2013

References

Asami, R., Yamada, T., Iryu, Y., Quinn, T. M., Meyer, C. P., and Pauley, G.: Interannual and decadal variability of the western Pacific sea surface condition for the years 1787–2000: reconstruction based on stable isotope record from a Guam coral. J. Geophys. Res., 110, C05018, doi:10.1029/2004JC002555, 2005.

Bagnato, S., Linsley, B. K., Howe, S. S., Wellington, G. M., and Salinger, J.: Coral oxygen isotope records of interdecadal climate variations in the South Pacific Convergence Zone region, Geochem. Geophys. Geosys., 6, Q06001, doi:10.1029/2004GC000879, 2005.

Braganza, K., Gergis, J. L., Power, S. B., Risbey, J. S., and Fowler, A. M.: A multiproxy index of the El Niño-Southern Oscillation, AD 1525–1982, J. Geophys. Res., 114, D05106, doi:10.1029/2008JD010896, 2009.

Bunge, L. and Clarke, A. J.: A verified estimation of the El Niño index NINO3.4 since 1877, J. Climate, 22, 3979–3992, 2009.

Chan, J.: Tropical cyclone activity in the northwest Pacific in relation to the El Niño/Southern Oscillation phenomenon, Mon. Weather Rev., 113, 599–606, 1985.

Charles, C. D., Cobb, K., Moore, M. D., and Fairbanks, R. G.: Monsoon-tropical ocean interaction in a network of coral records spanning the 20th century, Mar. Geol., 201, 207–222, 2003.

Cobb, K., Charles, C. D., Cheng, H., and Edwards, R. L.: El Niño-Southern Oscillation and tropical Pacific climate during the last millenium, Nature, 424, 271–276, 2003.

Collins, M., An, S.-I., Cai, W., Ganachaud, A., Guilyardi, E., Jin, F.-F., Jochum, M., Lengaigne, M., Power, S., Timmermann, A., Vecchi, G., and Wittenberg, A.: The impact of global warming on the tropical Pacific ocean and El Niño, Nat. Geosci., 3, 391–397, 2010.

Cook, E. R.: Niño 3 Index reconstruction, in: International Tree-Ring Data Bank, IGBP PAGES/World Data Center-A for Paleoclimatology Data Contribution Series, 2000.

Cook, E. R., D'Arrigo, R. D., and Anchukaitis, K. J.: ENSO reconstructions from long tree-ring chronologies: unifying the differences, in: Talk Presented at a Special Workshop on Reconciling ENSO Chronologies for the Past 500 Years, held in Moorea, French Polynesia on 2–3 April 2008, 2008.

Danabasoglu, G., Bates, S., Briegleb, B. P., Jayne, S. R., Jochum, M., Large, W. G., Peacock, S., and Yeager, S. G.: The CCSM4 ocean component, J. Climate, 25, 1361–1389, 2012.

CPD
9, 2929–2966, 2013

DeLong, K. L., Quinn, T. M., Taylor, F. W., Lin, K., and Shen, C.-C.: Sea surface temperature variability in the southwest tropical Pacific since AD 1649, Nat. Clim. Change, 2, 799–804, doi:10.1038/NCLIMATE1583, 2012.

Delworth, T. L., Broccoli, A. J., Rosati, A., Stouffer, R. J., Balaji, V., Beesley, J. A., Cooke, W. F., Dixon, K. W., Dunne, J. P., Dunne, K. A., Durachta, J. W., Findell, K. L., Ginoux, P., Gnanadesikan, A., Gordon, C. T., Griffies, S. M., Gudgel, R., Harrison, M. J., Held, I. M., Hemler, R. S., Horowitz, L. W., Klein, S. A., Knutson, T. R., Kushner, P. J., Langenhorst, A. R., Lee, H.-C., Lin, S.-J., Lu, J., Malyshev, S., Milly, P. C. D., Ramaswamy, V., Russell, J. L., Schwarzkopf, M. D., Shevliakova, E., Sirutis, J. J., Spelman, M. J., Stern, W. F., Winton, M., Wittenberg, A. T., Wyman, B., Zeng, F., and Zhang, R.: GFDL's CM2 global coupled climate models, Part I: Formulation and simulation characteristics, J. Climate, 19, 643–674, 2006.

Deser, C., Phillips, A. S., Tomas, R. A., Okumura, Y. M., Alexander, M. A., Capotondi, A., Scott, J. D., Kwon, Y.-O., and Ohba, M.: ENSO and Pacific decadal variability in the Community Climate System Model Version 4, J. Climate, 25, 2622–2651, doi:10.1175/JCLI-D-11-00301.1, 2012.

Emile-Geay, J., Cobb, K. M., Mann, M. E., and Wittenberg, A. T.: Estimating tropical Pacific SST variability over the past millennium, Part 1: Methodology and validation, J. Climate, 26, 2302–2328, doi:10.1175/JCLI-D-11-00510.1, 2013a.

Emile-Geay, J., Cobb, K. M., Mann, M. E., and Wittenberg, A. T.: Estimating tropical Pacific SST variability over the past millennium, Part 2: Reconstructions and uncertainties, J. Climate, 26, 2329–2352, doi:10.1175/JCLI-D-11-00511.1, 2013b.

Evans, M., Kaplan, A., Cane, M. A., and Villalba, R.: Interhemispheric climate linkages, in: Globality and Optimality in Climate Field Reconstructions from Proxy Data, Cambridge Univ. Press, 53–72, 2001.

Evans, M., Kaplan, A., and Cane, M. A.: Pacific sea surface temperature field reconstruction from coral δ^{18}O data using reduced space objective analysis, Paleoceanography, 17, 1007, doi:10.1029/2000PA000590, 2002.

Isdale, P. J., Stewart, B. J., Tickle, K. S., and Lough, J. M.: Palaeohydrological variation in a tropical river catchment: a reconstruction using fluorescent bands in corals of the Great Barrier Reef, Australia, Holocene, 8, 1–8, doi:10.1191/095968398670905088, 1998.

Kaplan, A., Cane, M., Kushnir, Y., Clement, A., Blumenthal, M., and Rajagopalan, B.: Analyses of global sea surface temperature 1856–1991, J. Geophys. Res., 103, 567–589, 1998.

CPD
9, 2929–2966, 2013

Landrum, L., Otto-Bliesner, B. L., Wahl, E. R., Conley, A., Lawrence, P. J., Rosenbloom, N., and Teng, H.: Last Millennium Climate and Its Variability in CCSM4, J. Climate, 26, 1085–1111, doi:10.1175/JCLI-D-11-00326.1, 2013.

Larkin, N. K. and Harrison, D. E.: ENSO Warm (El Niño) and Cold (La Niña) event life cycles: ocean surface anomaly patterns, their symmetries, asymmetries, and implications, J. Climate, 15, 1118–1140, 2002.

Le Quesne, C., Stahle, D. W., Cleaveland, M. K., Therrell, M. D., Aravena, J. C., and Barichivich, J.: Ancient austrocedrus tree-ring chronologies used to reconstruct central chile precipitation variability from AD 1200 to 2000, J. Climate, 19, 5731–5744, doi:10.1175/JCLI3935.1, 2006.

Linsley, B. K., Wellington, G. M., and Schrag, D. P.: Decadal sea surface temperature variability in the subtropical south Pacific from 1726 to 1997 AD, Science, 290, 1145, doi:10.1126/science.290.5494.1145, 2000.

Li, J., Xie, S.-P., Cook, E. R., Huang, G., D'Arrigo, R., Lui, F., Ma, J., and Zheng, X.-T.: Interdecadal modulation of El Niño amplitude during the past millennium, Nat. Clim. Change, 1, 114–118, 2011.

Lough, J. M.: Tropical river flow and rainfall reconstructions from coral luminescence: Great Barrier Reef, Australia, Paleoceanography, 22, PA2218, doi:10.1029/2006PA001377, 2007.

Mann, M., Bradley, R. S., and Hughes, M. K.: Multiscale Variability and Global and Regional Impacts, in: Long-term Variability in the El Niño-Southern Oscillation and Associated Teleconnections, Cambridge Univ. Press, 357–412, 2000.

McGregor, S., Timmermann, A., and Timm, O.: A unified proxy for ENSO and PDO variability since 1650, Clim. Past, 6, 1–17, doi:10.5194/cp-6-1-2010, 2010.

Nicholls, N.: Predictability of interannual variations of Australian seasonal tropical cyclone activity, Mon. Weather Rev., 113, 1144–1149, 1985.

Neale, R. B., Richter, J., Park, S., Lauritzen, P. H., Vavrus, S. J. P., Rasch, J., and Zhang, M.: The mean climate of the Community Atmosphere Model (CAM4) in forced SST and fully coupled experiments, J. Climate, in press, 2013.

Newton, A., Thunell, R., and Stott, L.: Climate and hydrographic variability in the Indo-Pacific warm pool during the last millennium, Geophys. Res. Lett., 33, L19710, doi:10.1029/2006GL027234, 2006.

Power, S., Casey, T., Folland, C., Colman, A., and Mehta, V.: Interdecadal modulation of the impact of ENSO on Australia, Clim. Dynam., 15, 319–324, 1999.

CPD
9, 2929–2966, 2013

Quinn, T. M., Crowley, T. J., Taylor, F. W., Henin, C., Joannot, P., and Join, Y.: A multicentury stable isotope record from a New Caledonia coral: interannual and decadal sea surface temperature variability in the southwest Pacific since 1657 AD, Paleoceanography, 13, 412–426, 1998.

Rayner, N., Parker, D., Horton, E., Folland, C., Alexander, L., Rowell, D., Kent, E., and Kaplan, A.: Global analyses of sea surface temperature, sea ice, and night marine air temperature since the late nineteenth century, J. Geophys. Res., 108, 4407, doi:10.1029/2002JD002670, 2003.

Sachs, J. P., Sachse, D., Smittenberg, R. H., Zhang, Z., Battisti, D. S., and Golubic, S.: Southward movement of the Pacific intertropical convergence zone AD 1400–1850, Nat. Geosci., 2, 519–525, doi:10.1038/NGEO554, 2009.

Smith, R. D., Jones, P., Briegleb, B., Bryan, F., Danabasoglu, G., Dennis, J., Dukowicz, J., Eden, C., Fox-Kemper, B., Gent, P., Hecht, M., Jayne, S., Jochum, M., Large, W., Lindsay, K., Maltrud, M., Norton, N., Peacock, S., Vertenstein, M., and Yeager, S.: The Parallel Ocean Program (POP) reference manual, Los Alamos National Laboratory Tech. Rep. LAUR-10-01853, 141 pp., 2010.

Smith, T. M., Reynolds, R. W., Peterson, T. C., and Lawrimore, J.: Improvements to NOAA's historical merged land–ocean surface temperature analysis (1880–2006), J. Climate, 21, 2283–2296, 2008.

Stahle, D., D'Arrigo, R. D., Krusic, P. J., Cleaveland, M. K., Cook, E. R., Allan, R. J., Cole, J. E., Dunbar, R. D., Therrell, M. D., Gay, D. A., Moore, M. D., Stokes, M. A., Burns, B. T., Villanueva-Diaz, J., and Thompson, L. G.: Experimental dendroclimatic reconstruction of the Southern Oscillation, B. Am. Meteorol. Soc., 79, 2137–2152, 1998.

Timmermann, A., Jin, F.-F., and Abshagen, J.: A non-linear theory for El Niño bursting, J. Atmos. Sci., 60, 152–165, 2003.

Wilson, R., Cook, E., D'Arrigo, R., Riedwyl, N., Evans, M. E., Tudhope, A., and Allan, R.: Reconstructing ENSO: the influence of method, proxy data, climate forcing and teleconnections, J. Quaternary Sci., 25, 6–78, 2010.

Wittenberg, A.: Are historical records sufficient to constrain ENSO simulations?, Geophys. Res. Lett., 36, L12702, doi:10.1029/2009GL038710, 2009.

Wittenberg, A. T., Rosati, A., Lau, N.-C., and Ploshay, J. J.: GFDL's CM2 global coupled climate models, Part III: Tropical Pacific climate and ENSO, J. Climate, 19, 698–722, 2006.

CPD
9, 2929–2966, 2013

Wolff, C., Haug, G. H., Timmermann, A., Sinninghe Damsté, J. S., Brauer, A., Sigman, D. M., Cane, M. A., and Verschuren, D.: Reduced interannual rainfall variability in East Africa during the last Ice Age, Science, 333, 743–747, 2011.

Zhang, R. H., Rothstein, L. M., and Busalacchi, A. J.: Origin of upper-ocean warming and El Niño change on decadal scales in the tropical Pacific Ocean, Nature, 391, 87–883, 1998.

CPD
9, 2929–2966, 2013

Table 1. Existing ENSO reconstructions employed in this study. Note that these ENSO reconstructions have at least annual resolution and are pre-screened such that they have a correlation of at least 0.5 with the annual mean (July–June) observations of ENSO, represented by Niño 3.4 area-averaged (hereafter N34, 5° S–5° N, 120° W–170° W) SST anomalies (SSTA; Table 2). This correlation cutoff ensures the ENSO reconstruction provides a skillful estimate of ENSO variability, at least over the instrumental epoch.

	Reference	Period	Proxy type	Source region
Proxy 1	Stahle et al. (1998)	1706–1997	Tree-ring	Pacific Basin
Proxy 2	Cook (2000)	1408–1978	Tree-ring	North America
Proxy 3	Mann et al. (2000)	1650–1990	Mixed	Near global (tropics)
Proxy 4	Evans et al. (2001)	1590–1990	Tree-ring	America
Proxy 5	Evans et al. (2002)	1800–1990	Coral	Indo-Pacific Basin
Proxy 6	Cobb et al. (2003)	1635–1703 and 1886–1998	Coral	Central equatorial Pacific
Proxy 7	Cook (2008)	1300–1978	Tree-ring	North America
Proxy 8	Braganza et al. (2009)	1525–1982	Tree-ring	Pacific Basin
Proxy 9	Braganza et al. (2009)	1727–1982	Mixed	Pacific Basin
Proxy 10	McGregor et al. (2010)	1650–1977	Mixed	Near global (tropics)
Proxy 11	Wilson et al. (2010)	1850–1998	Coral	Eastern equatorial Pacific
Proxy 12	Wilson et al. (2010)	1540–1998	Coral	Indo-Pacific Basin
Proxy 13	Li et al. (2011)	900–2002	Tree-ring	North America
Proxy 14	Wolff et al. (2011)	1208–2005	Lake Varves	East Africa

CPD
9, 2929–2966, 2013

Table 2. Correlation coefficients calculated between the high pass filtered (HPF; 10 yr cutoff) annual mean proxy network-based ENSO reconstructions and HPF instrumental observations of Niño 3.4 region SSTA during the overlapping instrumental period. All correlations are statistically significant above the 99 % level. We note that this measure of statistical significance takes into account serial (auto-)correlation in the series, based on the reduced effective number of degrees of freedom outlined by Davis (1976).

	Observed Niño 3.4 region SSTA			
	HadISST Raynor et al. (2003)	ERSST V3 Smith et al. (2008)	Kaplan Kaplan et al. (1998)	Niño 3.4 SSTA (Bunge and Clarke 2009)
Proxy 1	0.74	0.75	0.76	0.73
Proxy 2	0.78	0.71	0.77	0.77
Proxy 3	0.77	0.76	0.75	0.76
Proxy 4	0.54	0.69	0.55	0.59
Proxy 5	0.74	0.78	0.72	0.71
Proxy 6	0.71	0.7	0.72	0.69
Proxy 7	0.76	0.74	0.75	0.73
Proxy 8	0.63	0.58	0.59	0.64
Proxy 9	0.69	0.66	0.66	0.69
Proxy 10	0.83	0.83	0.82	0.82
Proxy 11	0.58	0.65	0.56	0.62
Proxy 12	0.58	0.59	0.6	0.61
Proxy 13	0.53	0.48	0.55	0.54
Proxy 14	0.54	0.57	0.54	0.58

CPD
9, 2929–2966, 2013

Table 3. The single station (SS) temperature and/or rainfall proxies employed in this study. Note that these proxies have at least annual resolution and are pre-screened such that they have a correlation of at least 0.3 with the annual mean (July–June) observations of ENSO, represented by Niño 3.4 area-averaged (hereafter N34, 5° S–5° N, 120° W–170° W) SST anomalies (SSTA; Table 4). This correlation cutoff ensures that the proxies provide a reasonably skillful estimate of ENSO variability over the instrumental epoch.

	Reference	Period	Proxy type	Location	Source region	Lat	Lon
SS proxy 1	Cook et al. (2004, 2008)	0–2006	Tree ring width	NADA PDSI	North America	27° N	255° E
SS proxy 2	LeQuesne et al. (2006)	1000–2000	Tree ring width	Chilean Cordillera	South America	33° S	288° E
SS proxy 3	ITRDB extraction	1675–1998	Tree ring width	Madera Canyon	Mexico	29° N	257° E
SS proxy 4	ITRDB extraction	1553–1998	Tree ring width	Nevado de Colima	Mexico	20° N	256° E
SS proxy 5	ITRDB extraction	1376–1998	Tree ring width	Cerro Baraja	Mexico	26° N	254° E
SS proxy 6	ITRDB extraction	1376–1999	Tree ring width	Cerro Baraja	Mexico	26° N	254° E
SS proxy 7	ITRDB extraction	1644–1998	Tree ring width	Creel Int. Airport	Mexico	28° N	252° E
SS proxy 8	ITRDB extraction	1481–1998	Tree ring width	El Salto	Mexico	24° N	254° E
SS proxy 9	ITRDB extraction	1583–1998	Tree ring width	El Tabacote/Tomochic	Mexico	28° N	252° E
SS proxy 10	ITRDB extraction	1712–1998	Tree ring width	Capote Knob	Texas, USA	29° N	262° E
SS proxy 11	ITRDB extraction	1473–1998	Tree ring width	Camp Spring	Texas, USA	29° N	257° E
SS proxy 12	ITRDB extraction	1473–1998	Tree ring width	Camp Spring	Texas, USA	29° N	257° E
SS proxy 13	Asami et al. (2005)	1790–2000	Coral δ^{18}O)	Double Reef	Guam	13° N	144° E
SS proxy 14	Bagnato et al. (2005)	1776–2001	Coral δ^{18}O)	Savusavu Bay	Fiji	16° S	179° E
SS proxy 15	DeLong et al. (2012)	1648–2000	Coral (Sr/Ca)	Amédée Island	New Caledonia	22° S	166° E
SS proxy 16	Isdale et al. (2001)	1644–1986	Coral (Fluorescence)	Havannah Island	Great Barrier Reef	18° S	146° E
SS proxy 17	Isdale et al. (2001)	1737–1980	Coral (Fluorescence)	Pandora Reef	Great Barrier Reef	18° S	146° E
SS proxy 18	Linsley et al. (2000)	1727–1997	Coral (Sr/Ca)	Rarotonga	Cook Islands	21° S	159° W
SS proxy 19	Lough et al. (2007)	1631–2005	Coral (Fluorescence)	Queensland River Flow	Great Barrier Reef	17–23° S	146–151° E
SS proxy 20	Quinn et al. (1998)	1657–1992	Coral δ^{18}O)	Amédée Island	New Caledonia	22° S	166° E
SS proxy 21	Charles et al. (2003)	1782–1990	Coral δ^{18}O)	Lombok Straight	Indonesia	8° S	115° E

CPD
9, 2929–2966, 2013

Table 4. Correlation coefficients with zero lag, and lead and lag times of one year (t-1 means proxy data lagging observed ENSO), calculated between the high pass filtered (HPF; 10 yr cutoff) annual mean single station proxy network (Table 3) and HPF instrumental observations of Niño 3.4 region SSTA during the overlapping instrumental period. The maximum absolute correlation for each observational product is highlighted by bold font.

	Observed Niño 3.4 region SSTA											
	HadISST Raynor et al. (2003)			HadISST Smith et al. (2008)			HadISST Kaplan et al. (1998)			Niño 3.4 SSTA Bunge and Clarke, (2009)		
	$t-1$	t	$t+1$	$t-1$	t	$t+1$	$t-1$	t	$t+1$	$t-1$	t	$t+1$
SS proxy 1	0.12	**−0.61**	0.18	0.10	**−0.62**	0.23	0.11	**−0.61**	0.14	0.09	**−0.61**	0.20
SS proxy 2	−0.04	**0.29**	−0.19	0.06	0.21	**−0.26**	−0.04	**0.30**	−0.17	−0.03	**0.26**	−0.17
SS proxy 3	−0.25	**0.43**	−0.01	−0.21	**0.45**	−0.05	−0.21	**0.41**	0.00	−0.21	**0.44**	0.00
SS proxy 4	−0.01	**0.32**	−0.09	−0.14	**0.31**	0.02	−0.02	**0.33**	−0.08	0.00	**0.29**	−0.13
SS proxy 5	−0.33	**0.43**	−0.05	−0.29	**0.42**	−0.16	−0.32	**0.40**	−0.04	−0.29	**0.43**	−0.08
SS proxy 6	−0.33	**0.46**	−0.07	−0.30	**0.44**	−0.18	−0.33	**0.42**	−0.06	−0.30	**0.45**	−0.10
SS proxy 7	−0.21	**0.43**	−0.19	−0.23	**0.41**	−0.24	−0.20	**0.40**	−0.15	−0.19	**0.41**	−0.19
SS proxy 8	−0.24	**0.55**	−0.11	−0.14	**0.47**	−0.19	−0.22	**0.48**	−0.09	−0.20	**0.50**	−0.13
SS proxy 9	−0.27	**0.49**	−0.12	−0.26	**0.50**	−0.22	−0.25	**0.47**	−0.09	−0.25	**0.48**	−0.14
SS proxy 10	**−0.27**	0.24	0.07	−0.28	**0.33**	0.02	**−0.27**	0.22	0.09	−0.22	**0.26**	0.04
SS proxy 11	−0.24	**0.40**	0.01	−0.22	**0.45**	−0.08	−0.22	**0.38**	0.03	−0.23	**0.42**	−0.02
SS proxy 12	−0.23	**0.38**	0.03	−0.21	**0.47**	−0.11	−0.20	**0.37**	0.03	−0.20	**0.39**	0.00
SS proxy 13	**0.43**	0.04	−0.09	**0.53**	0.10	−0.10	**0.38**	0.07	−0.11	**0.43**	0.07	−0.07
SS proxy 14	**0.59**	0.24	−0.34	**0.65**	0.23	−0.37	**0.57**	0.26	−0.30	**0.58**	0.26	−0.32
SS proxy 15	−0.03	**−0.50**	−0.16	−0.04	**−0.45**	−0.14	−0.01	**−0.47**	−0.15	−0.06	**−0.48**	−0.12
SS proxy 16	**−0.42**	0.14	0.30	**−0.34**	0.10	0.28	**−0.40**	0.13	0.31	**−0.38**	0.21	0.24
SS proxy 17	**−0.34**	0.15	0.30	−0.21	0.14	**0.23**	**−0.30**	0.18	0.27	**−0.26**	0.22	0.21
SS proxy 18	−0.07	**−0.44**	0.03	−0.18	**−0.50**	0.15	−0.09	**−0.43**	0.02	−0.08	**−0.44**	0.03
SS proxy 19	**−0.30**	0.08	0.24	**−0.30**	0.05	0.27	**−0.30**	0.12	0.28	**−0.26**	0.15	0.20
SS proxy 20	0.15	**0.28**	−0.06	**0.25**	0.18	−0.04	0.15	**0.26**	−0.05	0.15	**0.31**	−0.07
SS proxy 21	−0.12	**0.37**	0.10	−0.01	**0.35**	0.01	−0.10	**0.38**	0.10	−0.08	**0.42**	0.10

CPD
9, 2929–2966, 2013

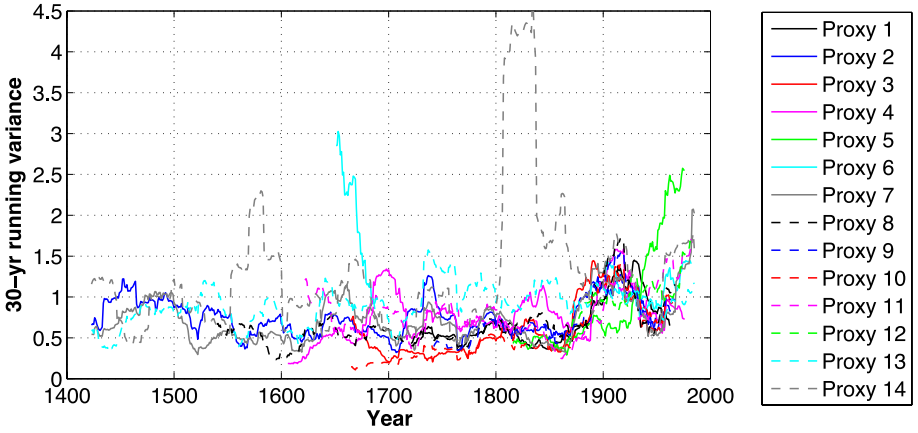

Fig. 1. The 30 yr running variance of each of the 14 high-pass filtered (HPF, 10 yr cutoff) ENSO reconstructions (see Table 1 for proxy details). Note the individual time proxy series were normalized over the period 1900–1977 prior to calculating the running variance in a 30 yr sliding window.

CPD
9, 2929–2966, 2013

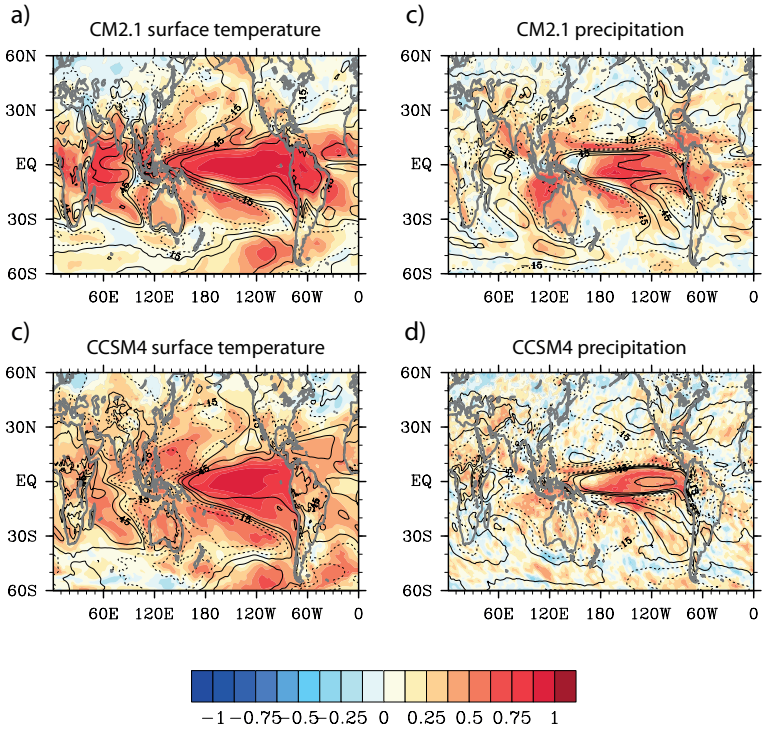

Fig. 2. The overlying black contours in panels **(a)** and **(b)** represent the correlation between the 2000 yr CM2.1 simulation HPF annual mean (July–June) anomalies of surface temperature (T_S) and rainfall, respectively, with the annual mean N34 SSTA. Contours are from −0.75 to 0.75 with a spacing of 0.3 and negative contours are dashed. Background shading indicates the correlation between the 2000 yr CM2.1 simulation 30 yr running variance of the high pass filtered (HP; 10 yr cutoff) annual mean (July–June) **(a)** T_S and **(b)** rainfall with the running variance of the HPF annual mean N34 SSTA. **(c)** and **(d)** as in **(a)** and **(b)**, respectively, but for 1000 yr CCSM4 model output.

CPD
9, 2929–2966, 2013

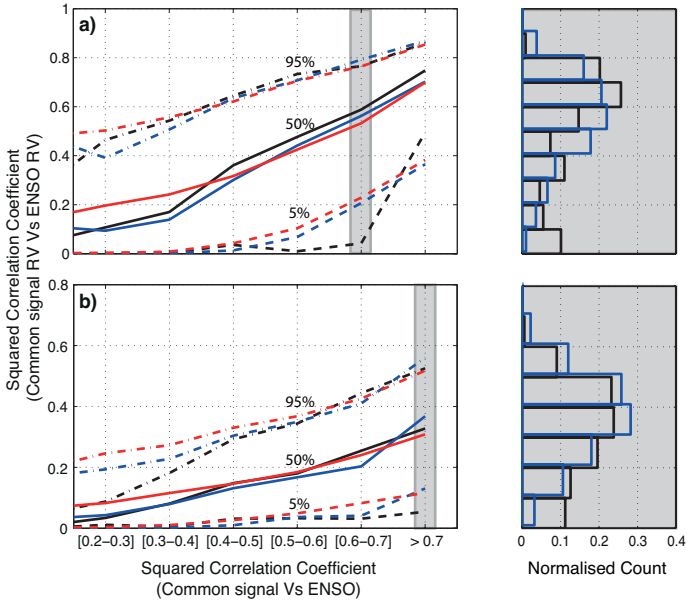

Fig. 3. (a) The 5 % (dashed line plus +'s), 50 % (solid line) and 95 % (dashed lines plus x's) percentiles of squared correlation coefficients calculated between CM2.1 precipitation running variance and the running variance of ENSO, binned against the squared correlation between precipitation and ENSO. The color of the lines indicates the number of source locations utilized in the precipitation signal, with black, blue and red lines corresponding to one, two and five source locations. The inset histogram displays the distribution of squared correlation coefficients calculated between precipitation running variance and the running variance of ENSO from the identified x-axis (grey shading) bin. **(b)** as in **(a)** but for CCSM4 model output. Note the different y-axis for panels **(a)** and **(b)**.

CPD
9, 2929–2966, 2013

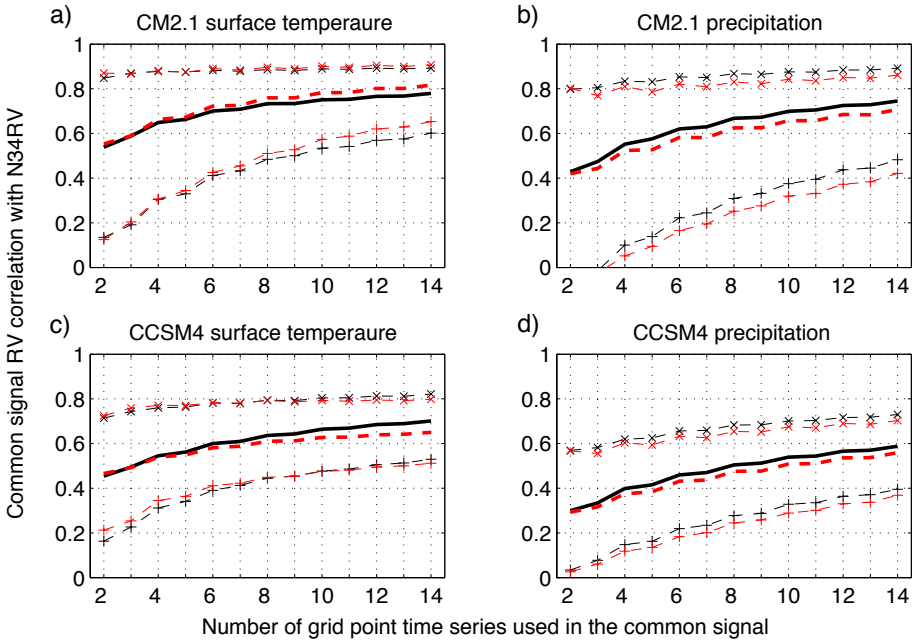

Fig. 4. (a) The 5 % (dashed line plus +'s), 50 % (solid line) and 95 % (dashed lines plus x's) of the correlation coefficients calculated between the CM2.1 MRV surface temperature and ENSO running variance (N34RV) are displayed in red, while those of the RVM surface temperature are displayed in black. **(b)** as in **(a)** but for the CM2.1 precipitation data. **(c)** and **(d)** as in **(a)** and **(b)** but for CCSM4 surface temperature and precipitation data respectively. The x-axis in each panel displays the number of grid point time series used to calculate the common signal.

CPD
9, 2929–2966, 2013

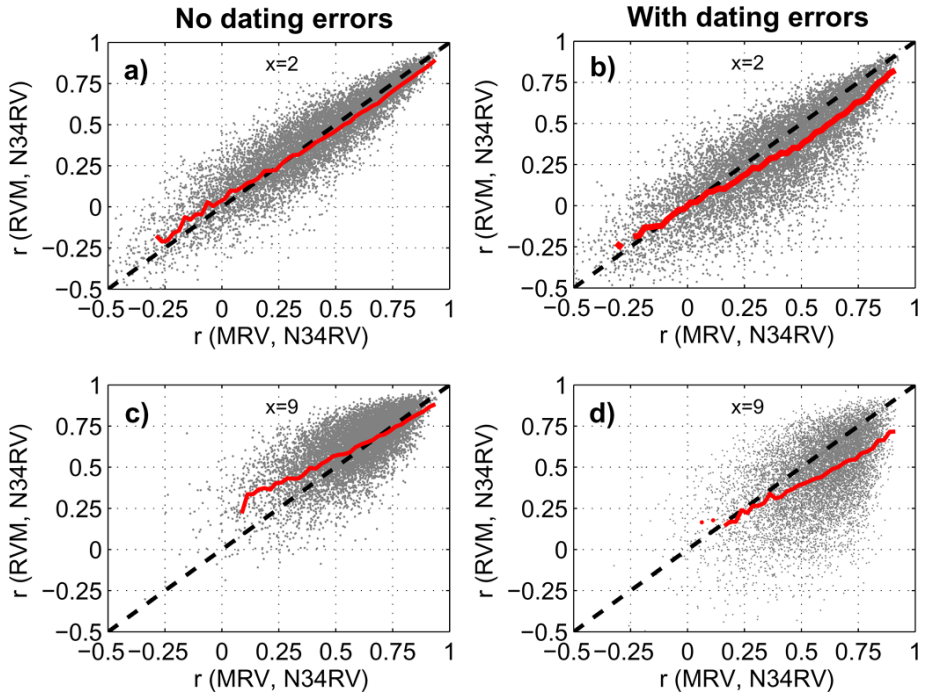

Fig. 5. (a) The correlation between CM2.1 rainfall MRV and ENSO running variance (denoted N34RV) plotted against the correlation between CM2.1 rainfall RVM and ENSO running variance for the case with only two members ($x = 2$). Panel **(c)** displays the same fields, however in this case x=9. **(b)** and **(d)** as in **(a)** and **(c)** but 1/2 of all rainfall time series include an introduced temporal shift to mimic a proxy dating error. The black dashed line in all panels represents the one-to-one line, while the solid red line represents the mean RVM value calculated in bins with width 0.025. Note that the mean values are only plotted when the bin contains a minimum of 20 RVM values.

CPD
9, 2929–2966, 2013

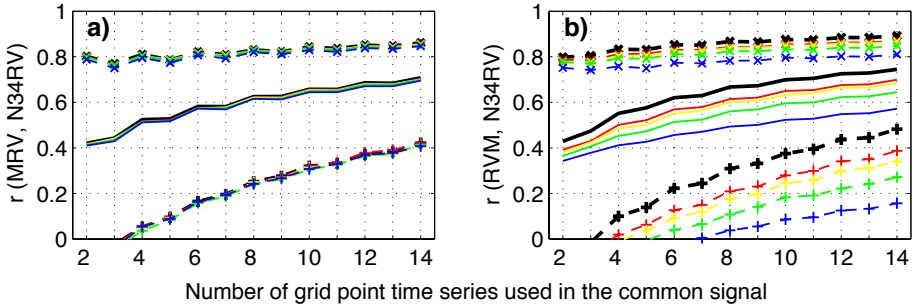

Fig. 6. (a) The 5 % (dashed line plus +'s), 50 % (solid line) and 95 % (dashed lines plus x's) of the correlation coefficients calculated between the CM2.1 rainfall MRV and ENSO running variance, while **(b)** displays the percentiles of correlation coefficients calculated between CM2.1 rainfall RVM and ENSO running variance. The black lines indicate those percentiles using data with no introduced temporal shifts, while the red, yellow, green and blue line respectively represent those percentiles using data with 1/5, 1/4, 1/3, 1/2 of the time series including an introduced temporal shift.

CPD
9, 2929–2966, 2013

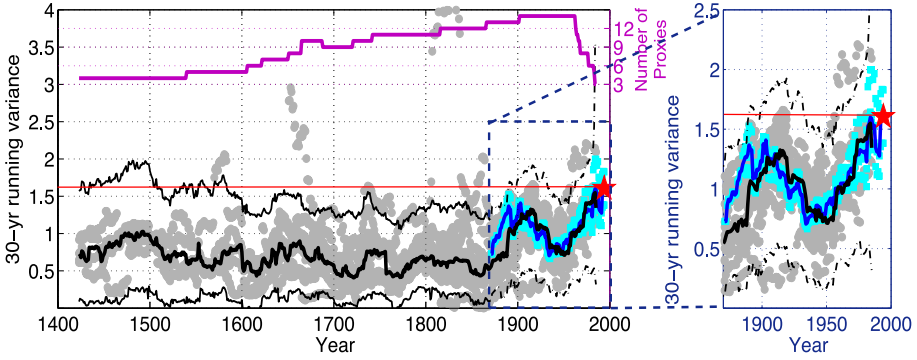

Fig. 7. The 30 yr running variance (grey dots) of each of the 14 high-pass filtered (HPF, 10 yr cutoff) ENSO reconstructions, overlaid with the MRV (thick black line). At any point in time prior to the observation period, the thin black linesrepresent the widest median running variance signal error bars of the two types of error analysis detailed in the Appendix A. Inside the window of instrumental data these error bars change to thin black dash-dot lines, as we have a direct measurement of ENSOs variance. The width of each of these two error bar estimates varies depending on the number of ENSO variance proxies available (see purple line at top of panel). Cyan dots indicate the 30 yr running variance of the 4 observed HPF Niño 3.4 SST anomalies, while the blue line represents the observed ensemble median running variance. The red star indicates the most recen value of the ensemble median 30 yr running variance of the 4 observed HPF Niño 3.4 SST anomalies (1979–2009), while the thin red line just extends this most recent value back through time, for comparison with the ensemble median proxy running variance and its error bars.

CPD
9, 2929–2966, 2013

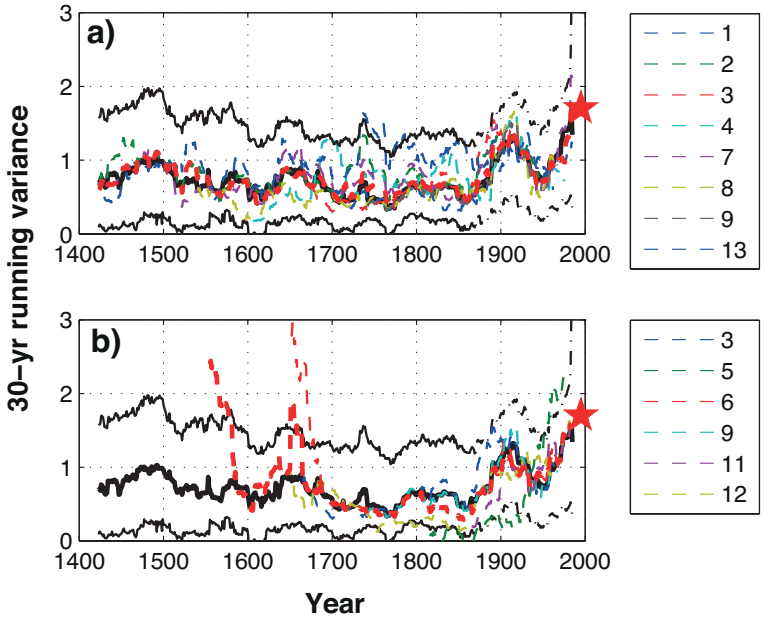

Fig. 8. (a) The 30 yr running variance of each of the 8 HPF (10 yr cutoff) ENSO reconstructions with common tree ring source proxies (proxy numbers correspond to those in Table 1), overlaid with the corresponding ensemble median running variance (thick dashed red line). **(b)** The 30 yr running variance of each of the 6 HPF (10 yr cutoff) ENSO reconstructions with common tropical coral reconstructions (proxy numbers in legend correspond to those in Table 1), overlaid with the corresponding ensemble median running variance (thick dashed red line). The underlying thick black line in both panels represents the median running variance of all 14 HPF (10 yr cutoff) ENSO reconstructions presented in Fig. 7, while the thin black lines represent the accompanying running variance signal error bars. The red star indicates the most recen value of the ensemble median 30 yr running variance of the 4 observed HPF Niño 3.4 SST anomalies.

CPD
9, 2929–2966, 2013

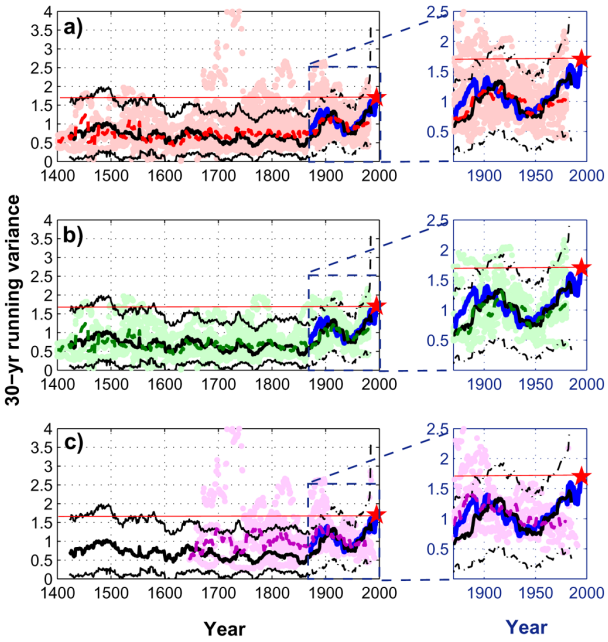

Fig. 9. (a) The 30 yr running variance (pink dots) of each of the 21 single station proxies (Table 3) overlaid with the ensemble median running variance (thick dashed red line). **(b)** The running variance of the 12 single station tree ring proxies (light green dots) with the median (thick green dashed line) overlaid, while **(c)** displays the running variance of the 9 single station coral proxies (light purple dots) with the median (thick purple dashed line) overlaid. The thick black line in both panels represents the median running variance of all 14 HPF (10 yr cutoff) ENSO reconstructions presented in Fig. 7, while the thin black lines represent the accompanying running variance signal error bars. The blue line represents the observed ensemble median running variance and the red star indicates its most recent value, while the thin red line just extends this most recent value back through time for comparison with the ensemble median proxy running variance.

CPD
9, 2929–2966, 2013